An International Journal of Optimization and Control: Theories & Applications
ISSN: 2146-0957 eISSN: 2146-5703
Vol.16, No.6, pp.2361-2377 (2026)
https://doi.org/10.36922/IJOCTA026300185

RESEARCH ARTICLE

Energy-storing analysis and fishtail stiffness optimization for a wire-driven elastic robotic fish

Xiaocun Liao*, Chao Zhou*, Junfeng Fan, Zhuoliang Zhang, Zhaoran Yin, and Liangwei Deng

The Laboratory of Cognition and Decision Intelligence for Complex Systems, Institute of Automation, Chinese Academy of Sciences, Beijing, China
liaoxiaocun2019@ia.ac.cn, chao.zhou@ia.ac.cn, junfeng.fan@ia.ac.cn, zhangzhuoliang2018@ia.ac.cn, yinzhaoran2021@ia.ac.cn, dengliangwei2020@ia.ac.cn

ARTICLE INFO

Article History:
Received: July 26, 2026
Revised: August 31, 2026
Accepted: September 11, 2026
Published Online: September 18, 2026

Keywords:
Wire-driven robotic fish
Stiffness optimization
Power fluctuations
Energy-storing
Controlled flexible unit

AMS Classification 2010:
70E60; 93C85; 70B15

ABSTRACT

The robotic fish with high propulsion efficiency and good maneuverability achieves underwater fishlike propulsion by commonly adopting a motor to drive the fishtail, causing significant fluctuations within motor power due to the uneven swing speed of the fishtail in one swing cycle. Hence, we propose a wire-driven robotic fish with a controlled flexible unit that is a spring-steel-based fishlike tail. This unit can produce elastic deformation to store energy under the action of the wire driving and motor to respond to fluctuations in motor power. Furthermore, we analyze the effects of the energy-storing of the controlled flexible unit on the smoothness of motor power. Based on the developed Lagrangian dynamic model and the cantilever beam model, the power-variance-based nonlinear optimization model for the stiffness of the controlled flexible unit is established to respond to sharp fluctuations in motor power during each fishtail swing cycle. The results validate that the energy-storing of the controlled flexible unit plays a vital role in improving the power fluctuations and maximum frequency of the motor by adjusting its stiffness reasonably, which is beneficial for achieving high propulsion and high speed for robotic fish. Compared with the rigid counterpart that is incapable of storing energy, the energy-storing of the controlled flexible unit is beneficial to increase the maximum frequency of the motor and the average thrust of the fishtail by 0.41 Hz and 0.06 N, respectively.

CC BY

1. Introduction

As human needs grow and robotics technology advances, robots are increasingly being integrated into everyday life and work, bringing us transformative benefits such as enhanced productivity, improved safety in hazardous environments, and personalized assistance in healthcare and education.[1–3] An increasing number of advanced technologies, such as reinforcement learning,[4,5] multimodal perception,[6,7] and intelligent planning and control,[8,9] are being integrated into these robots to cope with the complex demands of real-world environments.

In the field of marine development, the ocean contains abundant resources that humans can exploit. With the development of robotics, various robots have been applied to replace humans in underwater work. Compared with the traditional propeller-based underwater robot, the bionic robotic fish features high propulsion efficiency and good maneuverability by imitating fish swimming, and holds promising potential for underwater applications.[10,11]

*Corresponding Author

Recently, various robotic fishes, which are usually based on discrete joints,[12,13] fluid-driven modes,[14–17] smart materials,[18–21] magnetic actuators,[22,23] and tensegrity joints,[24,25] have been developed successfully. Clapham *et al.* proposed the robotic fish named iSplash-I, which reached a frequency of 6.6 Hz and a maximum speed of 2.8 BL/s. Based on the iSplash-I, the iSplash-II was further developed, which achieved a frequency of 20 Hz and a speed of 11.6 BL/s.[13] Using fluidic elastomer actuators, Marchese *et al.* developed a soft robotic fish capable of escape maneuvers.[16] A self-powered soft robot driven by the dielectric elastomer actuator was used to explore the Mariana Trench.[20] In addition, the wire-driven robotic fish has also attracted extensive attention.[26–30] Li *et al.* developed a wire-driven robotic fish, whose fishtail could swing in any direction.[26] The fishtail consisted of seven vertebrae that were connected by ball hinges, and two pairs of wires were mounted perpendicularly to drive the fishtail. A wire-driven robotic fish with an active body and compliant tail was proposed by Zhong *et al.*, and it was capable of achieving an average turning speed of 63 °/s and a maximum swimming speed of 2.15 BL/s.[27] Shintake *et al.* presented a wire-driven robotic fish with tensegrity systems, which could tune body stiffness by adjusting the cross-section and prestretch ratio of the cables.[29]

To improve the swimming performance of robotic fish, such as swimming speed and propulsion efficiency, many efforts have focused on exploring the passive flexible unit (PFU).[31–34] Through the interaction between the fishtail and the fluid, the PFU can periodically store and release energy through elastic deformation, which is beneficial for improving propulsion performance. Hence, the stiffness of the PFU can be tuned to improve the propulsion performance of robotic fish. Park *et al.* explored the influences of the PFU on thrust and verified that an optimal stiffness maximizes thrust at a given frequency.[31] Inspired by the caudal fin of fish, Reddy N *et al.* studied the influence of the stiffness distribution of the passive caudal fin on thrust and determined the optimal stiffness distribution of the caudal fin based on the developed optimization model.[32] Chen *et al.* adopted double torsion springs to design the PFU and verified that the PFU was beneficial for obtaining high swimming speed, high thrust, and low COT.[33] The robotic fish with pectoral fins driven by a passive flexible rowing joint was proposed by Behbahani *et al.*[34] Based on the developed dynamic model and experiments, the locomotion performance and propulsion efficiency were improved by adjusting the length and stiffness of the passive flexible joint.

The PFU, whose deformation is passively generated by the action of hydrodynamic forces, has a counterpart known as the controlled flexible unit (CFU). Unlike the PFU, the elastic deformation of the CFU arises from the active action of the drive mechanism, and its magnitude is controllable. Driving mechanisms such as wire driving and bar driving are usually powered by a motor. To imitate the continuum fishtail, the CFU has also been widely used in robotic fish.[35–40] For example, Li *et al.* designed a wire-driven robotic fish with a continuum fish tail, whose fishlike spine was an elastic-plate-based controlled flexible unit.[35] The robotic fish was driven by a wire pair to obtain the C-shape swing, and was capable of achieving a speed of 0.254 BL/s. A robotic shark that adopted an elastic beam and plate to simulate the fish spine was developed by Lau *et al.*, and the elastic beam serving as the CFU was driven by two pairs of wires.[36] Due to the double-wire driving, the robotic shark, whose fishtail could swing asymmetrically, was capable of achieving forward motion as well as ascending motion. To imitate carangiform swimming, a robotic fish, whose continuum fishtail contained a section of the polystyrene-chloride-sheet-based controlled flexible unit and was driven by the L-shaped metal bar and wire, was designed by Fujiwara *et al.*[37] Similar studies can be found in the literature.[38–40] Although the CFU has been widely applied to achieve a continuum fishtail in robotic fish, studies involving detailed analysis of the new advantages brought by the CFU and the optimization of the CFU are worthy of further exploration.

For robotic fish, the motor power exhibits a periodic sinusoid-like pattern due to the characteristics of the biomimetic undulation movement. Hence, the motor power undulates sharply under external disturbances, and the instantaneous maximum power can easily exceed the allowable power value of the motor, causing damage to the motor. Moreover, motor performance is also limited, which hinders improvements in the maximum swing frequency and swimming speed of robotic fish.

The main purpose of this paper is to address motor power fluctuations by optimizing the stiffness of the CFU to reduce power variance. The CFU equipped by the robotic fish can lower the peak and fill the valley of motor power through energy storage and release within one swing cycle, thereby effectively responding to motor power fluctuations and protecting the motor from damage. However, maximizing the advantages of the CFU's energy storage is challenging. In this paper, we focus on a wire-driven elastic robotic fish, whose fishlike tail

is based on dual spring steel and includes a CFU and a PFU. We analyze the effects of the CFU's energy storage on the smoothness of motor power. Based on the Lagrangian dynamic model and the cantilever beam model, a power-variance-based nonlinear optimization model of the CFU's stiffness is established to achieve stable motor power, where the swing frequency and the PFU's stiffness are taken into account. Extensive simulations are conducted and validate that the CFU's energy storage and stiffness do not contribute to the average power of the motor but affect the smoothness of motor power. Compared with a rigid counterpart incapable of storing energy, the CFU's stiffness can be tuned to make motor power more stable through periodic energy storage, which is beneficial for improving the maximum frequency of the motor and the swimming performance of robotic fish.

The rest of this paper is organized as follows. The mechanism design and dynamic modeling of robotic fish are provided in Section 2. Section 3 presents the analysis of energy storage and the nonlinear stiffness optimization for the CFU. The results are presented in Section 4. Finally, Section 5 summarizes the conclusions and future work.

2. Mechanism design and dynamic modeling

This section introduces the mechanism design and dynamic model of the wire-driven elastic robotic fish, which lays the foundation for the following optimization.

2.1. Design of robotic fish

To emulate fish swimming, a wire-driven robotic fish is developed, which includes a rigid fish head, an efficient transmission mechanism, a CFU, a PFU, and a rigid caudal fin, as shown in **Figure 1**. The transmission mechanism plays a significant role in transforming the circumferential rotation of the motor into the fishlike back-and-forth swing. Specifically, the L-shaped eccenter, one end of which is inserted into the slide way and the other end of which is connected to the output shaft of the motor, is driven by the motor. The eccenter further drives the pendulum bar through the slide way to obtain the fishlike swing, and the reel also rotates together with the pendulum bar because of the fixed connection.

The CFU and PFU together form the elastic fishtail of the robotic fish. The CFU is based on trapezoidal spring steel and driven by a wire. The PFU is a rectangular spring steel. When the reel rotates back and forth, the length of the wire on both sides of the fishtail changes periodically, resulting in the fishlike swing of the elastic fishtail. When the fishtail swings, the PFU periodically produces elastic deformation to store energy due to hydrodynamic forces, which is beneficial for improving swimming performance, such as swimming speed and propulsion efficiency. Hence, the PFU's stiffness can be tuned to affect its elastic deformation and the swimming performance of robotic fish.[33]

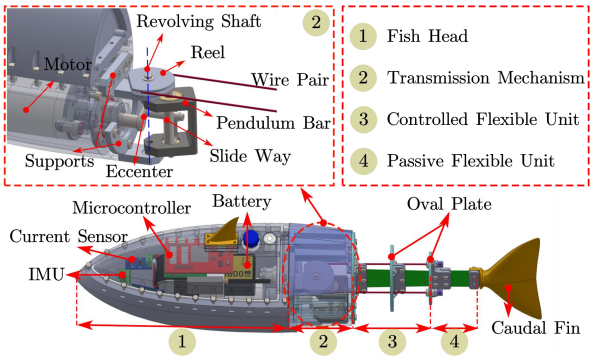


Figure 1. Overview design of the wire-driven elastic robotic fish

Unlike the PFU, the CFU can generate elastic deformation to achieve periodic energy storage under the action of the wire. Assuming that the output torque of the motor and the tension of the wire are large enough, the magnitude of elastic deformation of the CFU does not depend on its stiffness. That is because the deformation of the CFU depends on the change in wire length. As long as the length of the wire on both sides of the fishtail is given, the deformation of the CFU can be uniquely determined, regardless of its stiffness. It means that the swing law of the fishtail is also independent of the CFU's stiffness. In other words, the CFU's stiffness does not affect the swimming speed of the robotic fish. Given that the elastic potential energy of the CFU is provided by the motor, this paper focuses on exploring the advantages of the CFU's energy storage for the motor power of robotic fish and realizes the optimal design of the CFU's stiffness.

2.2. Dynamic model

In our previous study,[41] we developed a dynamic model for the robotic fish in free-swimming conditions, which was validated by aquatic experimental data. Given the bioinspired swing of the robotic fish, the fish head always exhibits periodic oscillatory motion at the same frequency and amplitude, which can act as a buffer and, to some extent, reduce the motor output torque and power. To fully ensure the reliability and stability of the

robotic fish, it is necessary to ignore the periodic oscillatory motion of the fish head and consider the maximum possible load on the motor. Therefore, based on the free-swimming dynamic model presented in our previous study,[41] we establish a dynamic model with the fish head fixed and the fishtail swinging in order to optimize the CFU's stiffness. Although the model has been simplified to some extent(specifically, the fish head is fixed and greater emphasis is placed on the fishtail swing), the fishtail shape and swing pattern remain unchanged, and all previously calibrated hydrodynamic and physical parameters have been retained.

2.2.1. Coordinate frames

For the continuum fishtail, we make the following two assumptions. First, the shape of the CFU is an arc after bending, which can be replaced by the corresponding chord in the dynamic model. Second, the PFU is modeled as a torsion spring since its length is much less than the body length.

The inertial reference frame $C_w = \{O - XYZ\}$ and link-fixed reference frame $C_i = \{O_i - X_iY_iZ_i\}$ (i = 1,2), which are attached to the links L_i, are defined in **Figure 2**. Note that the CFU is denoted as $\hat{L}_1$, and L_1 and L_2 denote the chord of the CFU and the caudal fin, respectively. l_i, w_i, h_i and m_i represent the length, width, height and mass of the link L_i, respectively. $l_{T,i}$, $w_{T,i}$, and $d_{T,i}$ denote the length, width, and thickness of the i-th spring steel ($i = 1$: CFU, $i = 2$: PFU), respectively. E_i, and I_{Zi} denote the elastic modulus and the area moment of inertia of the i-th spring steel, respectively. The angle between the axis X and X_i is denoted as θ_i. φ_1 is the angle of the axis X and X_1, and φ_2 is the angle of the axis X_2 and X_1. β denotes the central angle of $\hat{L}_1$ and is positive when the CFU bends to the right.

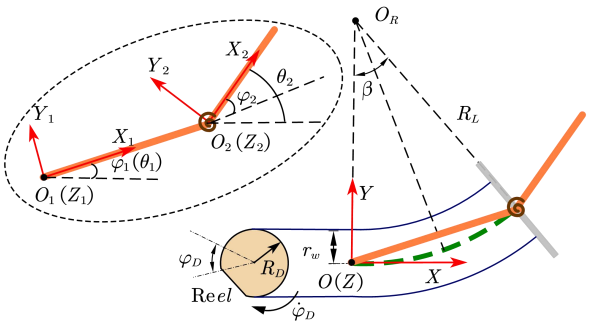


Figure 2. Definition of coordinate frames. The green dotted line denotes the CFU. The two orange solid lines represent the chord of the CFU and the caudal fin, respectively. The PFU is simplified as the torsion spring.

2.2.2. Kinematics model

According to the transmission mechanism, the angle of the reel is calculated as

$$\varphi_D = \arcsin\left(d_1 \sin(\varphi_m)/d_2\right), \tag{1}$$

where d_1 and d_2 represent the offset of the eccenter and the distance between the revolving shaft and the slide way, respectively; φ_m denotes the angle of the motor and is given by $\varphi_m = \omega t$; ω is the angular velocity of the motor. Based on **Figure 2**, the wire can also be divided into two sections, and the length of the wire is obtained as:

$$\Delta l_w = R_D\varphi_D = R_L\beta - 4(R_L - r_w)\sin(\beta/4), \tag{2}$$

$$l_1 = 2R_L \sin(\beta/2) = 2l_{T,1}\sin(\beta/2)/\beta, \tag{3}$$

where R_D and r_w denote the radius of the reel and the distance between the body axis and the wire pair, respectively; R_L is the arc radius of the CFU. The angles θ_1 and θ_2 are given by $\theta_1 = \varphi_1 = \beta/2$, and $\theta_2 = \theta_1 + \varphi_2$, respectively.

Furthermore, the generalized vector $\boldsymbol{q} = [q_1\ q_2]^T = [\varphi_1\ \varphi_2]^T$ is defined, and the linear and angular velocities of the center of mass of the link L_i are formulated as follows:

$${}^w\boldsymbol{v}_1 = \boldsymbol{J}_{v1}\dot{\boldsymbol{q}},\ {}^w\boldsymbol{v}_2 = \boldsymbol{J}_{v2}\dot{\boldsymbol{q}}, \tag{4}$$

$${}^w\boldsymbol{\omega}_1 = \boldsymbol{J}_{\omega1}\dot{\boldsymbol{q}},\ {}^w\boldsymbol{\omega}_2 = \boldsymbol{J}_{\omega2}\dot{\boldsymbol{q}}, \tag{5}$$

$$\boldsymbol{J}_{v1} = \begin{bmatrix} -l_{c,1}\sin q_1 & 0 \\ l_{c,1}\cos q_1 & 0 \\ 0 & 0 \end{bmatrix}, \tag{6}$$

$$\boldsymbol{J}_{v2} = \begin{bmatrix} -l_1\sin q_1 - l_{c,2}\sin(q_1+q_2) & -l_{c,2}\sin(q_1+q_2) \\ l_1\cos q_1 + l_{c,2}\cos(q_1+q_2) & l_{c,2}\cos(q_1+q_2) \\ 0 & 0 \end{bmatrix}, \tag{7}$$

$$\boldsymbol{J}_{\omega1} = \begin{bmatrix} 0 & 0 \\ 0 & 0 \\ 1 & 0 \end{bmatrix},\ \boldsymbol{J}_{\omega2} = \begin{bmatrix} 0 & 0 \\ 0 & 0 \\ 1 & 1 \end{bmatrix}, \tag{8}$$

where $\boldsymbol{J}_{vi}$ and $\boldsymbol{J}_{\omega i}$ are the Jacobian matrices of the link L_i; $l_{c,i}$ denotes the distance between the center of mass of the link L_i and O_i.

2.2.3. Lagrangian dynamic modeling

The Lagrangian function Υ is defined as the difference between the kinetic energy E_k and the potential energy E_p, which is calculated as

$$\Upsilon = E_k - E_p, \tag{9}$$

$$E_k = \frac{1}{2}\sum_{i=1}^{2}\left({}^w\boldsymbol{v}_i^T\boldsymbol{M}_i\,{}^w\boldsymbol{v}_i + {}^w\boldsymbol{\omega}_i^T\boldsymbol{I}_i\,{}^w\boldsymbol{\omega}_i\right), \tag{10}$$

$$E_p = E_{pfu} = \frac{1}{2}\kappa_2\theta_s^2, \tag{11}$$

where $\boldsymbol{M}_i$ and $\boldsymbol{I}_i$ denote the mass matrix and the inertia tensor of L_i, respectively; E_{pfu} represents the elastic potential energy of the PFU; θ_s represents the PFU's bend angle and is equal to

$\varphi_2 - \beta/2$; κ_2 denotes the torsional spring constant or the PFU's stiffness, and is calculated as

$$\kappa_2 = \frac{E_2 I_{Z2}}{l_{T,2}} = \frac{E_2 w_{T,2} d_{T,2}^3}{12 l_{T,2}}. \tag{12}$$

As analyzed in Section 2.1, the CFU's stiffness does not affect the swimming speed of the robotic fish, which is why the Lagrangian function excludes the CFU's elastic potential.

Finally, the dynamic model is given by

$$\frac{d}{dt}\frac{\partial \Upsilon}{\partial \dot{\boldsymbol{q}}} - \frac{\partial \Upsilon}{\partial \boldsymbol{q}} = [\tau_{J1} + \tau_{Hd,1},\ \tau_{Hd,2}]^T, \tag{13}$$

where τ_{J1} denotes the equivalent joint torque used to drive the link L_1, and $\tau_{Hd,i}$ represents the generalized torque of the hydrodynamic force with respect to O_i.

2.2.4. Hydrodynamic force analysis

According to the drag force theory, the added mass force ${}^w\boldsymbol{F}_{a,i}$ and the drag forces ${}^w\boldsymbol{F}_{d,i}$ of the link L_i are calculated as

$${}^w\boldsymbol{F}_{a,i} = -m_{a,i}\ {}^w\dot{\boldsymbol{v}}_i, \tag{14}$$

$${}^w\boldsymbol{F}_{d,i} = {}^w\boldsymbol{R}_i \begin{bmatrix} -\frac{1}{2}\rho c_{f,i} S_{x,i}\ {}^i v_{x,i} |{}^i v_{x,i}| \\ -\frac{1}{2}\rho c_{d,i} S_{y,i}\ {}^i v_{y,i} |{}^i v_{y,i}| \\ 0 \end{bmatrix}, \tag{15}$$

respectively, where the added mass $m_{a,i}$ is equal to the product of m_i and the added mass coefficient $c_{m,i}$; ${}^w\dot{\boldsymbol{v}}_i$ and ${}^i\boldsymbol{v}_i = [{}^i\boldsymbol{v}_{x,i}\ {}^i\boldsymbol{v}_{y,i}\ 0]^T$ are the acceleration and velocity of the center of mass of L_i, respectively, and the left superscript w and i denote the reference frame C_w and C_i, respectively; $S_{x,i}$ and $S_{y,i}$ denote the characteristic areas of L_i on the X_i and Y_i axes, respectively; $c_{d,i}$ and $c_{f,i}$ denote the drag coefficient and friction coefficient of L_i, respectively; ρ denotes the fluid density; ${}^w\boldsymbol{R}_i$ denotes the rotation matrix of C_i with respect to C_w, and can be expressed as

$${}^w\boldsymbol{R}_i = \begin{bmatrix} \cos\theta_i & -\sin\theta_i & 0 \\ \sin\theta_i & \cos\theta_i & 0 \\ 0 & 0 & 1 \end{bmatrix}. \tag{16}$$

Hence, the hydrodynamic force of the link L_i is given by

$${}^w\boldsymbol{F}_{ad,i} = {}^w\boldsymbol{F}_{a,i} + {}^w\boldsymbol{F}_{d,i}. \tag{17}$$

Furthermore, the $\tau_{Hd,1}$ and $\tau_{Hd,2}$ can be expressed as follows:

$$\tau_{Hd,1} = \boldsymbol{k}^T({}^w\boldsymbol{r}_{cm1} \times {}^w\boldsymbol{F}_{ad,1} + {}^w\boldsymbol{r}_{cm2} \times {}^w\boldsymbol{F}_{ad,2}), \tag{18}$$

$$\tau_{Hd,2} = \boldsymbol{k}^T\left[({}^w\boldsymbol{r}_{cm2} - {}^w\boldsymbol{r}_{O_2}) \times {}^w\boldsymbol{F}_{ad,2}\right], \tag{19}$$

where ${}^w\boldsymbol{r}_{cmi}$ denotes the position of the center of mass of the link L_i in C_w;${}^w\boldsymbol{r}_{O_2}$ represents the position of O_2 in C_w; $\boldsymbol{k}$ is equal to $[0\ 0\ 1]^T$.

Based on **Equations (13)**, **(18)** and **(19)**, we can obtain the real-time states of the robotic fish, e.g., θ_s, τ_{J1}, which are affected by the frequency f, and the PFU's stiffness κ_2. Based on the above dynamic model, the output torque and power of the motor can be further obtained by incorporating the force models of the CFU and transmission mechanism, and the power-variance-based nonlinear optimization model can be established to optimize the CFU's stiffness.

3. Energy storage analysis and stiffness optimization model of CFU

This section focuses on the functions of the CFU's energy storage, and further derives the nonlinear optimization model of the CFU's stiffness by combining the developed dynamic model with the force models of the CFU and the transmission mechanism. Note that the CFU's stiffness is calculated as

$$\kappa_1 = \frac{E_1 I_{Z1}}{l_{T,1}} = \frac{E_1 w_{T,1} d_{T,1}^3}{12 l_{T,1}}, \tag{20}$$

and we adjust the CFU's stiffness by changing its thickness $d_{T,1}$ in this paper.

3.1. Analysis of the CFU's energy storage

More attractively, the CFU can store and release energy periodically due to elastic deformation. Based on the cantilever beam model, the bending moment and the elastic potential energy of the CFU are given by

$$T_{e,1} = \kappa_1 \beta = \frac{\beta E_1 w_{T,1} d_{T,1}^3}{12 l_{T,1}}, \tag{21}$$

$$E_{cfu} = \frac{1}{2}\kappa_1 \beta^2 = \frac{\beta^2 E_1 w_{T,1} d_{T,1}^3}{24 l_{T,1}}, \tag{22}$$

respectively.

To explore the effects of the CFU's energy storage on motor power, the swing process of the fishtail in one cycle is analyzed, as shown in **Figure 3**. It is obvious that the angular acceleration $\dot{\omega}'$ points toward the initial position of the body axis owing to the sinusoid-like swing of the fishtail. The direction of the angular acceleration and hydrodynamic forces (including F_{tail} and F_{fin}) remains coincident during the drive stroke and opposite during the recovery stroke, which results in a difference in motor torque between the two strokes. Specifically, the motor torque during the drive stroke is significantly less than that during the recovery stroke, and the motor power exhibits a similar trend to the motor torque.

Interestingly, the output power of the motor increases significantly during the drive stroke since

the CFU needs to store energy provided by the motor. On the contrary, the CFU returns to the equilibrium state and releases the stored elastic potential energy during the recovery stroke, which can reduce the output power of the motor. Hence, for the whole swing cycle, the output power of the motor becomes more stable owing to the CFU's energy storage. Given that the energy storage capability of the CFU is directly related to its stiffness, we will establish the stiffness optimization model with the aim of improving the smoothness of the output power of the motor.

3.2. Nonlinear optimization model for the CFU's stiffness

Based on the above dynamic model, the equivalent joint torque τ_{J1} can be obtained. Obviously, the equivalent torque generated by the pulling force of the wire is equal to the sum of the equivalent joint torque of the link L_1 and the bending moment of the CFU, that is,

$$T_{wire,eq} = \tau_{J1} + T_{e,1}. \tag{23}$$

Hence, the pulling force of the wire is given by

$$F_{wire} = \frac{T_{wire,eq}}{r_w}, \tag{24}$$

where positive and negative F_{wire} represent the pulling force of the right and left wires, respectively. The torque generated by the wire with respect to the reel is given by

$$T_{wire,r} = F_{wire} R_D. \tag{25}$$

Treating the reel, slide way, and pendulum bar as a single rigid body and neglecting the self-rotation of the slide way, we can formulate the dynamic model of the transmission mechanism according to the law of rotation, that is,

$$\begin{aligned} &-\frac{T_m}{d_1 \cos\varphi_m} d_2 \cos\varphi_D + T_{wire,r} \\ &= (J_R + J_S + J_P)\ddot{\varphi}_D, \end{aligned} \tag{26}$$

where J_R, J_S, and J_P denote the moments of inertia of the reel, slide way, and pendulum bar, respectively; T_m represents the motor torque, which is expressed as

$$\begin{aligned} &T_m = \\ &-\frac{-T_{wire,r} + (J_R + J_S + J_P)\ddot{\varphi}_D}{d_2 \cos\varphi_D} d_1 \cos\varphi_m. \end{aligned} \tag{27}$$

To make the motor power smoother, we establish the following nonlinear optimization model to minimize the variance of the motor power, that is,

$$\min_{\kappa_1} var(P_m(t))\|_0^t, \tag{28}$$

where $var(\cdot)\|_0^t$ represents the variance of $\cdot$ within the duration of $0-t$, and $P_m = T_m\omega$ denotes the motor power. It is evident that when the average power of the motor $\bar{P}_m$ remains constant, the smaller the variance of the motor power is, the more stable the motor power is, meaning that the peak-to-peak value and peak value of the motor power are smaller. Hence, it is beneficial to protect the motor from damage and improve the maximum output frequency. Similarly, the following optimization model can be adopted:

$$\min_{\kappa_1} \left\{ \max(P_m(t))\|_0^t - \min(P_m(t))\|_0^t \right\}, \tag{29}$$

where $\max(\cdot)\|_0^t$ and $\min(\cdot)\|_0^t$ represent the maximum and minimum values of $\cdot$ within the duration of $0-t$, respectively. Specifically, we can determine the CFU's stiffness range by

$$\kappa_1 \in \left\{ \kappa_1 | var(P_m(t))\|_0^t \le var_m \right\}, \tag{30}$$

where var_m denotes the allowable maximum variance of the motor power.

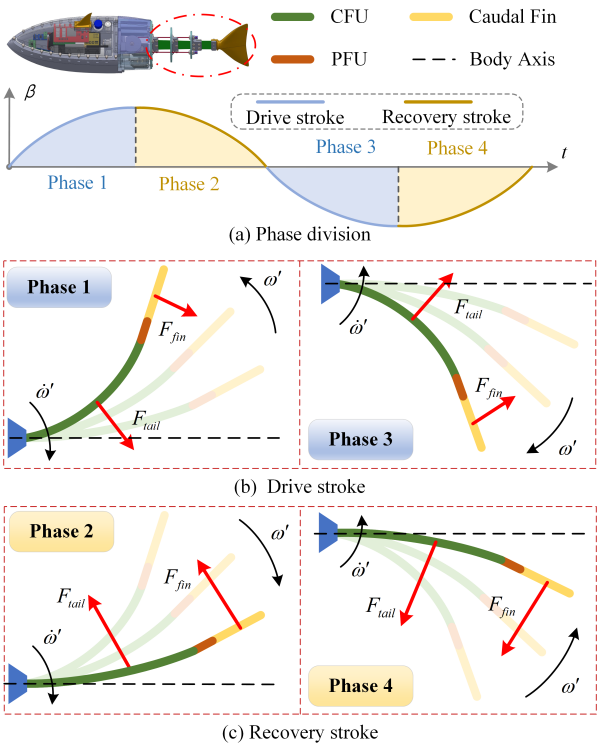


Figure 3. Swing analysis of the fishtail in one cycle. (a) The phase division of one cycle. The swing cycle of the fishtail includes (b) the drive stroke and (c) the recovery stroke. The drive stroke is defined as the duration when the fishtail swings from the middle to the sides, and the recovery stroke is opposite to the drive stroke. Here, F_{tail} and F_{fin} represent the hydrodynamic forces of the fishtail and caudal fin, respectively.

3.3. Determination of the CFU's stiffness range

For the above optimization model, a reasonable range of κ_1 should be determined. To calculate

the maximum κ_1, static analysis is adopted, that is, $\tau_{J1} = 0$ and $\ddot{\varphi}_D = 0$. The motor torque under static conditions can be expressed as

$$T_m^s = \frac{T_{e,1} R_D}{r_w d_2 \cos\varphi_D} d_1 \cos\varphi_m. \tag{31}$$

Obviously, the maximum κ_1 is determined as

$$\begin{aligned} &\kappa_1^{max} = \max\{\kappa_1\} \\ &s.t.\ \max(T_m^s) \le T_m^{max}, \end{aligned} \tag{32}$$

where T_m^{max} denotes the maximum torque that the motor can provide.

On the other hand, if a small κ_1 is used, the CFU is not capable of supporting the fishtail owing to the axial force from the caudal fin. In this case, there is unexpected deformation of the CFU, which affects the C-shape swing and amplitude of the fishtail. In this paper, we use the buckling of columns to determine the minimum κ_1 for given f and κ_2, that is,

$$\begin{aligned} &\kappa_1^{min}(f, \kappa_2) = \min\{\kappa_1\} \\ &s.t.\ \frac{\pi^2 E_1 I_{Z1}}{(\mu l_{T,1})^2} \ge F_{cr} \end{aligned} . \tag{33}$$

where μ represents the length factor and is equal to 2; F_{cr} denotes the axial force generated by the caudal fin during free swimming, and is calculated as

$$F_{cr} = \boldsymbol{i}^T [\ {}^1\boldsymbol{R}_w ({}^w\boldsymbol{F}_{a,2} + {}^w\boldsymbol{F}_{d,2})], \tag{34}$$

where $\boldsymbol{i} = [1\ 0\ 0]^T$, and ${}^1\boldsymbol{R}_w$ denotes the inverse matrix of ${}^w\boldsymbol{R}_1$.

Finally, the nonlinear optimization model **(28)** is rewritten as follows (for given f and κ_2):

$$\begin{aligned} &\min_{\kappa_1} var(P_m(t))\|_0^t \\ &s.t.\ \kappa_1^{min}(f, \kappa_2) \le \kappa_1 \le \kappa_1^{max} \end{aligned} . \tag{35}$$

Given that the aforementioned optimization model has only one variable (that is, the CFU's stiffness κ_1) to be optimized, we employ a traversal algorithm for a thorough sweep.

In the aforementioned modeling, we disregarded the friction loss caused by wire driving. The detailed analysis is as follows. According to the power formula, $P_f = N_m \mu F_{wire,N} V_{f,N}$, where N_m is the number of contact points between the wire and the oval plate, μ is the dynamic friction coefficient, $F_{wire,N}$ is the normal force exerted by the wire on the oval plate, and $V_{f,N}$ is the relative velocity between the wire and the oval plate. Equivalently, since the fishtail swings periodically and symmetrically, the friction loss between the wire and the oval plate is related to the frequency (which directly affects the relative velocity $V_{f,N}$) and the average pulling force of the wire. As discussed in Section 3.1, even if the CFU's stiffness varies, the average output torque (equivalently, the average pulling force of the wire) over one cycle remains unchanged for a given frequency and PFU's stiffness. Meanwhile, the proposed optimization model is formulated for a specified frequency and PFU's stiffness. That is to say, the friction loss does not vary with the CFU's stiffness and can be assumed constant , since both the frequency and PFU's stiffness are fixed in the proposed optimization model. Consequently, the influence of friction results only in an upward shift of the curves of average power/power variance versus CFU's stiffness, without changing the extremum of the power variance. It should be noted that friction loss is unavoidable.

4. Numerical simulation

To validate the proposed dynamic model and optimization model, extensive numerical simulations are conducted in this section. The parameters used in the simulation, including the physical parameters and hydrodynamic parameters, are presented in **Tables 1–3**. Note that the thickness resolution of the spring steel is usually 0.1 mm. All hydrodynamic parameters are derived from the previously calibrated values,[41] which were calibrated based on actual aquatic experimental data.

4.1. Simulation of fishtail swing

Based on the above dynamic model, the motor torque T_m and power P_m are obtained, as shown in **Figure 4**, where $f = 4$ Hz, $\kappa_1 = 0.15$ N·m, and $\kappa_2 = 1.31$ N·m. Due to the constant angular velocity of the motor, the curve of T_m follows the same law as that of P_m, and the average torque and average power of the motor are 0.1277 N·m and 3.21 W, respectively. The positive work of the motor is greater than the negative work, and the total work of the motor applied to drive the fishtail is greater than 0, which is in line with the objective law. In addition, according to **Figure 5**, it is observed that the phase of θ_2 lags behind that of θ_1 due to the PFU's elastic deformation, and the amplitudes of θ_s, θ_1, and θ_2 are 0.21 rad, 0.32 rad, and 0.68 rad, respectively.

Table 1. Physical parameters of the robotic fish

Name	m_i	l_i	h_i	w_i	$l_{c,i}$	$S_{x,i}$	$S_{y,i}$
$\hat{L_1}$	0.058	0.083	0.028	0.004	0.042	1.120	23.240
L_2	0.037	0.097	0.052	0.010	0.049	5.200	50.440
Unit	kg	m	m	m	m	cm^2	cm^2

Table 2. Physical parameters of the spring steel and the transmission mechanism

Name	$l_{T,1}$	$l_{T,2}$	$w_{T,1}$	$w_{T,2}$	E_i	J_R	J_S	J_P
Value	0.083	0.020	0.028	0.025	197000	5.49×10^{-6}	2.03×10^{-6}	4.61×10^{-5}
Unit	m	m	m	m	MPa	$kg \cdot m^2$	$kg \cdot m^2$	$kg \cdot m^2$

Table 3. Hydrodynamic parameters used in the simulation

Name	$c_{m,1}$	$c_{m,2}$	$c_{f,1}$	$c_{f,2}$	$c_{d,1}$	$c_{d,2}$
Value	0.30	0.30	0.35	0.62	4.71	4.78

Figure 6 presents the thrust curve of the robotic fish. The robotic fish faces the negative direction of the X-axis in the dynamic model. That is to say, when the fishtail swings, the robotic fish swims along the negative direction of the X-axis. As can be seen, the average thrust is -0.525 N, indicating that the thrust magnitude is 0.525 N and the thrust direction aligns with the negative direction of the X-axis. Since the fishtail swings symmetrically, the oscillation frequency of the thrust is twice the swing frequency of the fishtail. That is to say, when the fishtail finishes a drive stroke and a recovery stroke, the thrust undergoes an oscillation cycle. In addition, as can be seen from **Figure 6**, the thrust of the fishtail is mainly produced during the recovery stroke, while the drive stroke mainly provides the drag force, which is in line with **Figure 3**.

The stored energy E_{cfu} of the CFU is depicted in **Figure 7**, from which we observe that the period of the CFU's energy storage is 0.125 s, and the curve of E_{cfu} is similar to $|\sin(8\pi t)|$. Obviously, the CFU is capable of storing energy from the motor during the drive stroke, and the stored energy is released to drive the fishtail during the recovery stroke. The maximum elastic potential energy that the CFU can store is about 0.035 J in this case. As discussed in Section 3.1, the output power of the motor increases significantly during the drive stroke since the CFU needs to store energy provided by the motor. On the contrary, the CFU returns to the equilibrium state and releases the stored elastic potential energy during the recovery stroke, to reduce the torque required from the motor to maintain the kinematic trajectory. Hence, for the whole swing cycle, the output power of the motor becomes more stable owing to the CFU's energy storage.

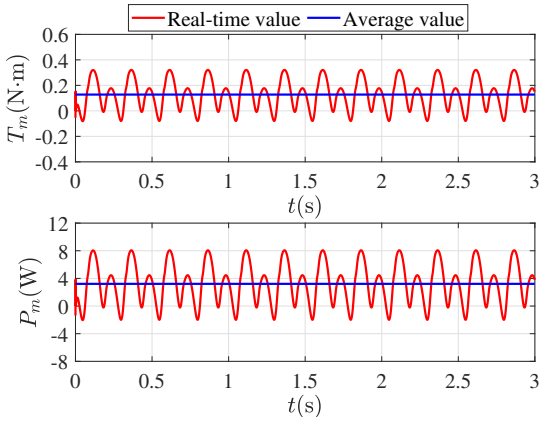


Figure 4. Real-time curves of motor torque T_m and power P_m. Here, f, κ_1, and κ_2 are 4 Hz, 0.15 N·m, and 1.31 N·m, respectively.

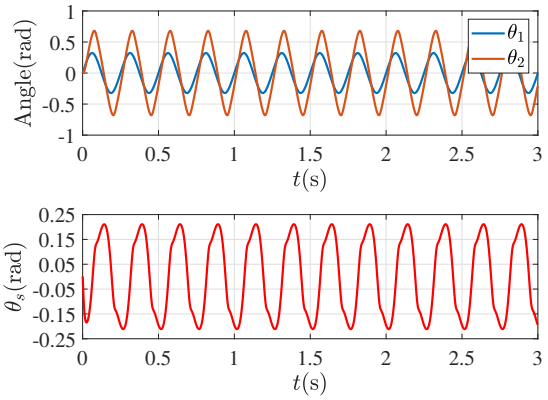


Figure 5. Curves of θ_1, θ_2 and θ_s. Here, f, κ_1, and κ_2 are 4 Hz, 0.15 N·m, and 1.31 N·m, respectively. The three curves follow a sine-like curve, which is in line with the swing rule of the fishtail.

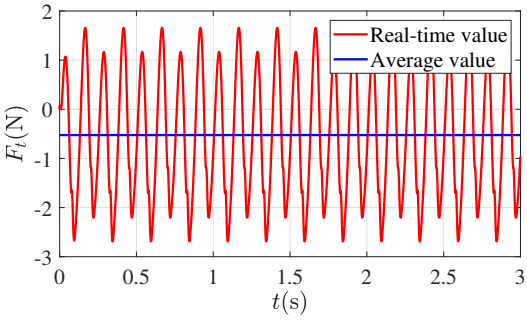


Figure 6. Thrust curves of the fishtail. Here, f, κ_1, and κ_2 are 4 Hz, 0.15 N·m, and 1.31 N·m, respectively.

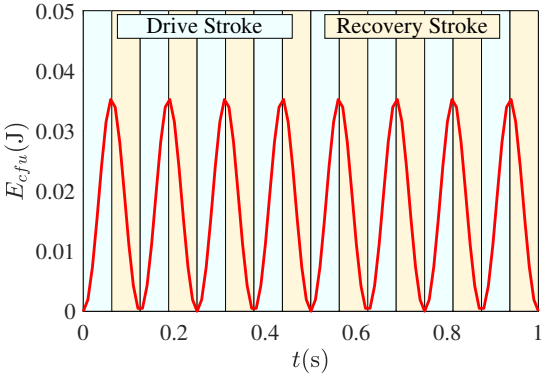


Figure 7. Stored energy of the CFU versus time. Here, f, κ_1, and κ_2 are 4 Hz, 0.15 N·m, and 1.31 N·m, respectively

To further validate the dynamic model, the changes in θ_s and the phase difference ϕ_s between θ_1 and θ_2 are explored, as shown in **Figures 8** and **9**. When κ_2 is relatively small (0.16 - 2.57 N·m), θ_s and ϕ_s increase significantly with increasing frequency, which is attributed to the increased deformation magnitude of the PFU due to the hydrodynamic forces of the caudal fin. For example, when κ_2 is 0.16 N·m, the minimum θ_s and ϕ_s are 0.059 rad and 0.003 rad, respectively, and the maximum θ_s and ϕ_s are 0.80 rad and 1.99 rad, respectively. The increments in θ_s and ϕ_s are 0.741 rad and 1.987 rad, respectively. However, when κ_2 is relatively large (2.57 - 10.51 N·m), θ_s increases slightly with increasing frequency. At $\kappa_2 = 10.51$ N·m, θ_s increases from 0.007 rad to 0.12 rad, and the absolute increment is equal to 0.113 rad. Similarly, ϕ_s increases from 0.003 rad to 0.14 rad, and the absolute increment is equal to 0.137 rad. This phenomenon occurs because the PFU's stiffness is very large, and it is difficult for the hydrodynamic force to bend and deform the PFU. It is obvious that the above results are consistent with the objective law, laying a solid foundation for the following optimization.

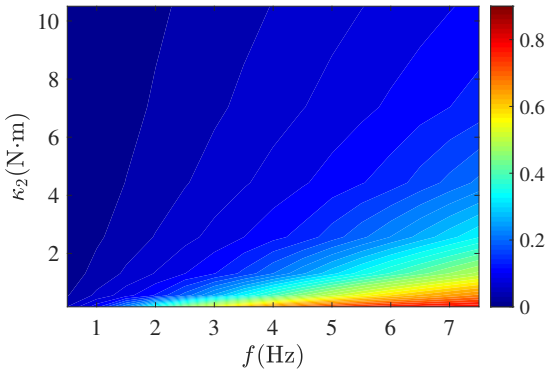


Figure 8. The PFU's angle θ_s (rad) versus f and κ_2

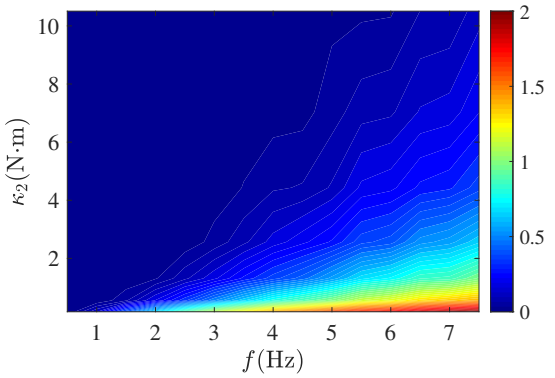


Figure 9. The phase difference ϕ_s (rad) between θ_1 and θ_2 versus f and κ_2

4.2. Validation of the CFU's stiffness range

In this section, we determine the maximum and minimum values of κ_1. First, according to **Equation (31)**, it is concluded that the bending moment of the CFU increases with κ_1, resulting in an increase in $\max(T_m^s)$. According to **Equation (32)**, we obtain $\kappa_1^{max} = 14.46$ N·m, based on the maximum output torque of the motor used, which is 3 N·m. Second, for different combinations of f and κ_2, we determine the minimum κ_1 according to **Equation (33)**, as depicted in **Figure 10**. There is a positive correlation between $\kappa_1^{min}(f, \kappa_2)$ and f at a given κ_2, which is attributed to the increased magnitude of the axial force acting on the CFU. The minimum and maximum values of $\kappa_1^{min}(f, \kappa_2)$ are 0.0011 N·m and 0.64 N·m, respectively.

According to **Equation (22)**, we can conclude that the maximum E_{cfu} exhibits a linear relationship with κ_1, and the maximum energies of the CFU for the minimum and maximum κ_1 are 2.5×10^{-4} J and 3 J, respectively. Obviously, by adjusting the CFU's stiffness, we can obtain a significant improvement in the energy storage capability of the CFU, which is why we adopt spring steel. The advantage is that when adjusting the

CFU's stiffness extensively to meet actual requirements, we do not need to redesign the robotic fish to meet assembly requirements, and the size and mass of the robotic fish also remain essentially constant.

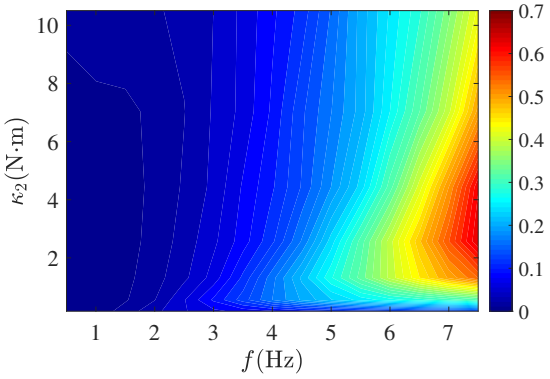
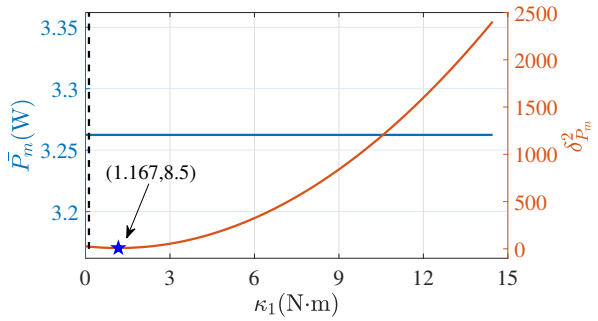


Figure 10. Curve of minimum κ_1 (N·m) at given f and κ_2

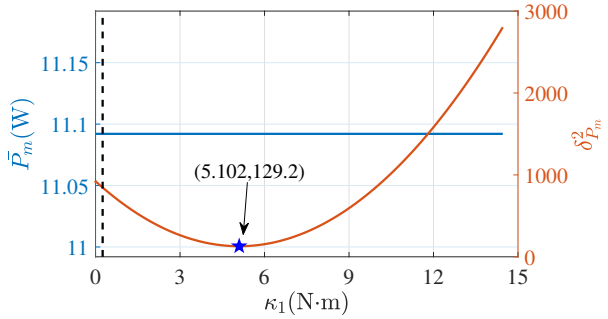
4.3. Validation of the CFU's stiffness optimization

Furthermore, we explore the effect of κ_1 on motor power for given f and κ_2, as shown in **Figure 11**. Obviously, κ_1 does not affect the average value $\bar{P}_m$ of the motor power, which confirms that the CFU's stiffness does not affect the swimming speed of the robotic fish. The average torque of the motor is also independent of κ_1 due to the constant angular velocity. However, κ_1 has a significant influence on the smoothness of the motor power, which is represented by the variance $\delta^2_{P_m}$. For example, according to **Figure 11a**, $\delta^2_{P_m}$ increases sharply for $f = 4$ Hz and $\kappa_2 = 2.57$ N·m, when κ_1 is greater than 3 N·m. This is because the CFU's bending moment increases sharply with increasing κ_1, which magnifies the peak value of the motor power and torque.

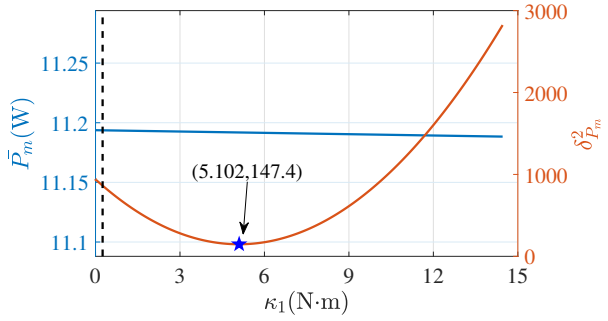
From **Figure 11**, the optimal κ_1 and the peak value of τ_{J1} are 1.167 N·m and 1.12 N·m, respectively, when $f = 4$ Hz and $\kappa_2 = 2.57$ N·m . However, the optimal κ_1 and the peak value of τ_{J1} are 5.102 N·m and 4.04 N·m, respectively, for $f = 6$ Hz and $\kappa_2 = 10.51$ N·m. This phenomenon means that the peak value of τ_{J1} also increases with increases in f and κ_2, and in order to minimize $\delta^2_{P_m}$, it is necessary to increase the CFU's stiffness and $T_{e,1}$ correspondingly to respond to the change in τ_{J1}. In addition, as can be seen from **Figure 11**, when f and κ_2 are given, $\delta^2_{P_m}$ first decreases and then increases with increasing κ_1, and there is an optimal solution κ_1^* that minimizes $\delta^2_{P_m}$.



(a) $f = 4$ Hz, $\kappa_2 = 2.57$ N·m.



(b) $f = 6$ Hz, $\kappa_2 = 10.51$ N·m.



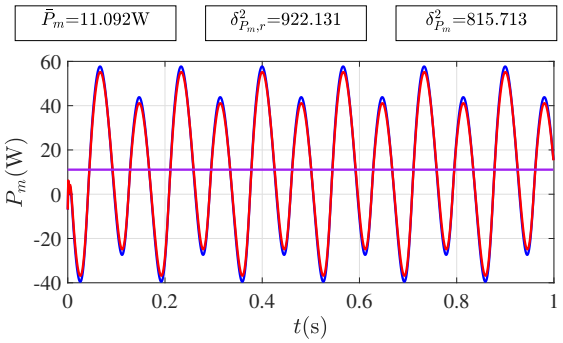
(c) $f = 6$ Hz, $\kappa_2 = 10.51$ N·m.

Figure 11. Average value $\bar{P}_m$ and variance $\delta^2_{P_m}$ of motor power versus κ_1. The black dotted line and the blue pentagram denote $\kappa_1^{min}(f, \kappa_2)$ and the optimal solution, respectively. (c) Sensitivity analysis. A disturbance with an average value of 0 and a variance of 0.1 is applied to the motor angle.

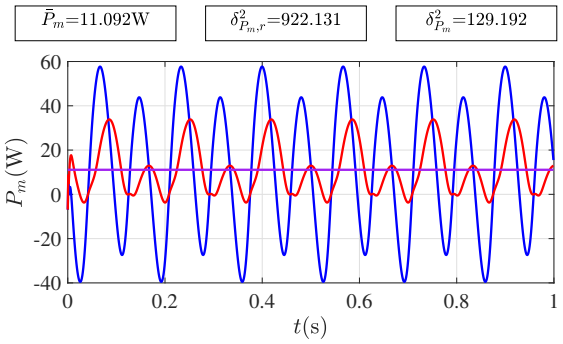
To assess the robustness of the optimized model, a disturbance with an average value of 0 and a variance of 0.1 is applied to the motor angle, and the result is shown in **Figure 11c**. By comparing **Figure 11b** with **Figure 11c**, the disturbance has an effect on both the average power and the power variance of the motor. The average power changes by approximately 0.1 W. The optimal variance increases from 129.2 to 147.4, indicating that the power variance is relatively sensitive to uncertain factors such as disturbances and noise. It is worth noting that the optimal CFU's stiffness barely changes and remains at 5.102 N·m after rounding. This is because the introduction of disturbance causes the real-time power to exhibit random fluctuations.

To illustrate the influence of κ_1 on the motor power intuitively, **Figure 12a–c** depict the real-time curves of the motor power when κ_1 is 0.35 N·m, 5.102 N·m, and 9.57 N·m, respectively, where $f = 6$ Hz and $\kappa_2 = 10.51$ N·m . Obviously, the average power $\bar{P}_m$ of the motor is 11.092 W, which is independent of κ_1. By contrast, $\delta^2_{P_m}$ exhibits large differences, and the minimum $\delta^2_{P_m}$ of 129.192 is obtained when κ_1 is 5.102 N·m. Comparing **Figure 12a**, **Figure 12b** and **Figure 12c**, it is found that when the variance of the motor power is small, the negative power is also significantly reduced. To maintain the same average power, the peak value of the motor power is correspondingly weakened, thereby reducing $\delta^2_{P_m}$ and improving the stability of the motor power. In addition, compared with the rigid counterpart that is incapable of storing energy, the CFU can lower the peak and fill the valley of motor power by energy storage and release to respond to motor power fluctuations effectively, if κ_1 is adjusted reasonably, as shown in **Figure 12b**. We use $\delta^2_{P_m,r}$ to denote the variance of the motor power for the rigid counterpart. Compared with the rigid counterpart, $\delta^2_{P_m}$ for the CFU with a stiffness of 5.102 N·m decreases by 85.99%. The appropriate κ_1 of the CFU is necessary for improving the power fluctuations. As can be seen from **Figure 12a** and **12c**, if κ_1 is relatively small or large, $\delta^2_{P_m}$ is approximately equal to $\delta^2_{P_m,r}$, and the motor power still fluctuates violently.

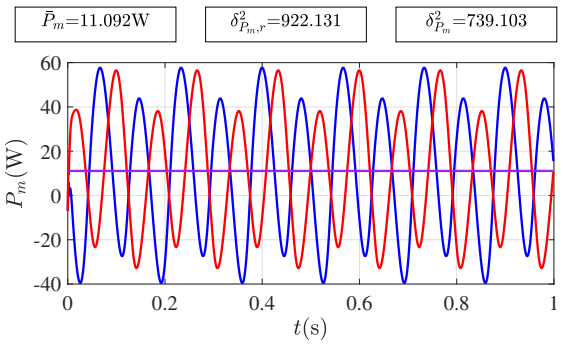
Furthermore, κ_1^* and the corresponding minimum variance are obtained by solving **Equation (35)**, as shown in **Figures 13** and **14**, respectively. **Figure 15** depicts the peak value of τ_{J1} at different f and κ_2. In **Figures 13, 14** and **15**, we traverse all suitable values of κ_2 (corresponding to thicknesses of 0.2:0.1:0.8 mm) to build a complete mapping relationship instead of focusing on the case at the optimal κ_2. This is because the optimization of κ_2 is not the focus of this paper. The optimal κ_2 can be obtained by optimizing the swimming performance (such as speed and thrust), which is an important direction for future work. According to **Figures 13** and **15**, it is found that κ_1^* increases with increasing f when κ_2 is relatively small, because the CFU's stiffness and bending moment need to be enhanced to respond to the increase in the peak value of τ_{J1} for maintaining smaller variances. In addition, it can be seen that κ_1^* increases at a given frequency as κ_2 increases, which is also attributed to the increase in the peak value of τ_{J1}. Over the considered ranges of f and κ_2, the minimum and maximum values of κ_1^* are 0.0443 N·m and 5.21 N·m, respectively, which are broadly consistent with the stiffness range selected in practice.



(a) $\kappa_1 = 0.35$ N·m



(b) $\kappa_1 = 5.102$ N·m.



(c) $\kappa_1 = 9.57$ N·m.

Figure 12. Real-time curves of motor power at different κ_1 within 0 - 1 s. Here, $f = 6$ Hz and $\kappa_2 = 10.51$ N·m. The red and blue curves represent the real-time motor power for the controlled flexible unit with the given stiffness κ_1 and the rigid counterpart, respectively.
Note that the three blue curves are identical in the three subgraphs. The purple line denotes the average power.

To validate the advantages of the CFU's energy storage, comparisons between the CFU and rigid counterpart in terms of the average value and variance of the motor power are performed, as shown in **Figure 16**, where the variances for the CFU are obtained by the nonlinear optimal model 35. It is obvious that the average power of the motor for the CFU is equal to that of the rigid counterpart, that is, the CFU's energy storage does not contribute to the propulsion performance of the

robotic fish. As can be seen from **Figure 16a**, both $\delta^2_{P_m}$ values for the CFU and rigid counterpart increase at small κ_2 as the frequency increases, and $\delta^2_{P_m}$ for the CFU is slightly smaller than that of the rigid counterpart. According to **Figure 15**, it is found that the peak values of τ_{J1} are relatively small, and the maximum value is about 2 N·m at $\kappa_2 = 1.31$ N·m, which results in a relatively small $\delta^2_{P_m}$ (less than 200). Hence, the CFU makes only a small contribution to reducing $\delta^2_{P_m}$ through its energy storage advantages. Since $\delta^2_{P_m}$ is relatively large at $\kappa_2 = 10.51$ N·m owing to the large peak values of τ_{J1}, the CFU's energy storage can adjust $\delta^2_{P_m}$ effectively.

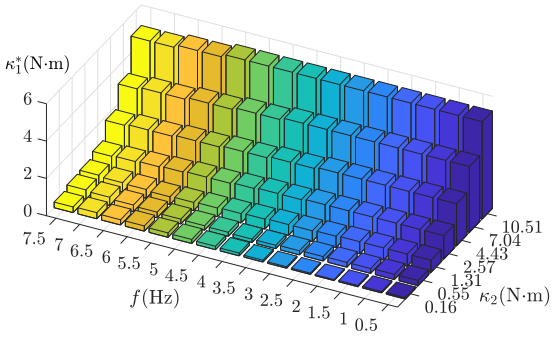


Figure 13. Optimal CFU's stiffness κ_1^* at different f and κ_2

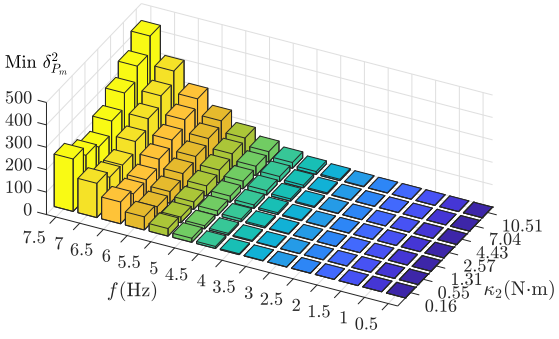


Figure 14. Minimum variance of motor power at different f and κ_2

To further evaluate the advantages of the CFU's energy storage, two indicators, namely, the relative decline ratio η_r and absolute decline value η_a of $\delta^2_{P_m}$ are defined as follows:

$$\eta_r = \frac{\delta^2_{P_m,r} - \delta^2_{P_m}}{\delta^2_{P_m,r}} \times 100\%, \tag{36}$$

$$\eta_a = \delta^2_{P_m,r} - \delta^2_{P_m}. \tag{37}$$

For example, when $f = 7.5$Hz and $\kappa_2 = 10.51$ N·m, respectively, $\delta^2_{P_m,r}$ and $\delta^2_{P_m}$ are equal to 1538 and 424.9, respectively, and η_r and η_a are 72.37% and 1113.1, respectively. **Figure 17** depicts the curves of η_r and η_a for different combinations of f and κ_2. It is obvious that, at a given frequency, the larger κ_2 is, the larger η_r and η_a are, which means that the CFU's energy storage plays a vital role in reducing the variance of the motor power. In addition, η_r decreases and η_a increases with increasing frequency when κ_2 is constant. In particular, the relative decline ratio approaches 100% as the frequency is relatively small.

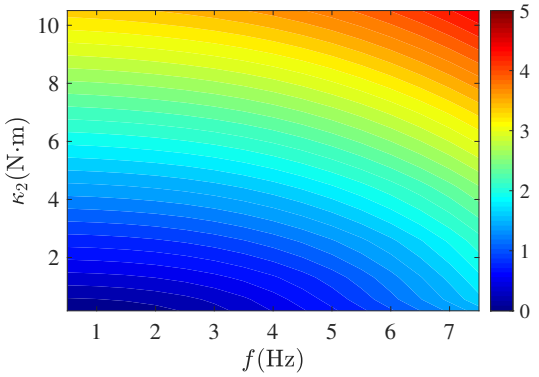
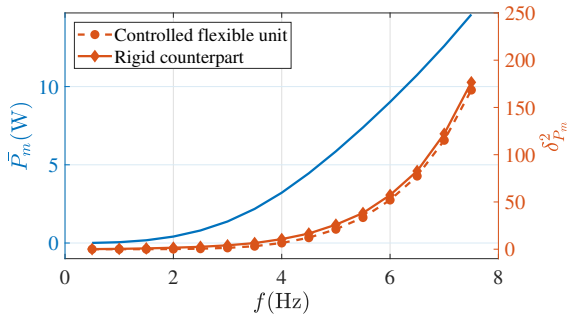
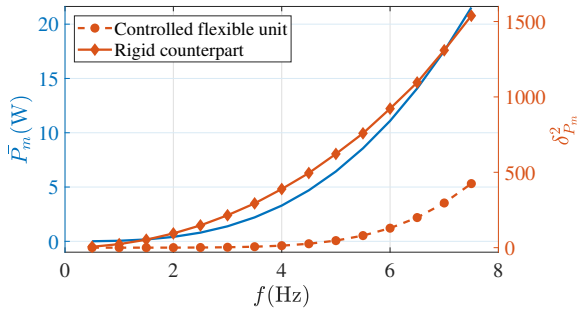


Figure 15. Peak value of τ_{J1} (N·m) at different f and κ_2



(a) $\kappa_2 = 1.31$ N·m.



(b) $\kappa_2 = 10.51$ N·m.

Figure 16. Comparison of average value $\bar{P}_m$ and variance $\delta^2_{P_m}$ of motor power between the CFU and rigid counterpart

As analyzed above, the stable output power of the motor is beneficial for improving the frequency. **Figure 18** presents the maximum power

of the motor for the CFU and rigid counterpart, where $\kappa_2 = 10.51$ N·m, and $\kappa_1 = \kappa_1^*$. Since the allowable power of the motor used is about 147.34 W, the highest frequencies of the motor for the CFU and rigid counterpart are about 10.47 Hz and 10.06 Hz, respectively, without damaging the motor. The relative increase in frequency is 4.1%, which is beneficial for improving the propulsion performance. For example, the thrust of the fish-tail improves from 3.60 N to 3.66 N, increasing by 0.06 N. In addition, when the frequency is 10.47 Hz, the maximum motor power decreases by 16.13 W (equivalent to 9.9%) due to the CFU's energy storage.

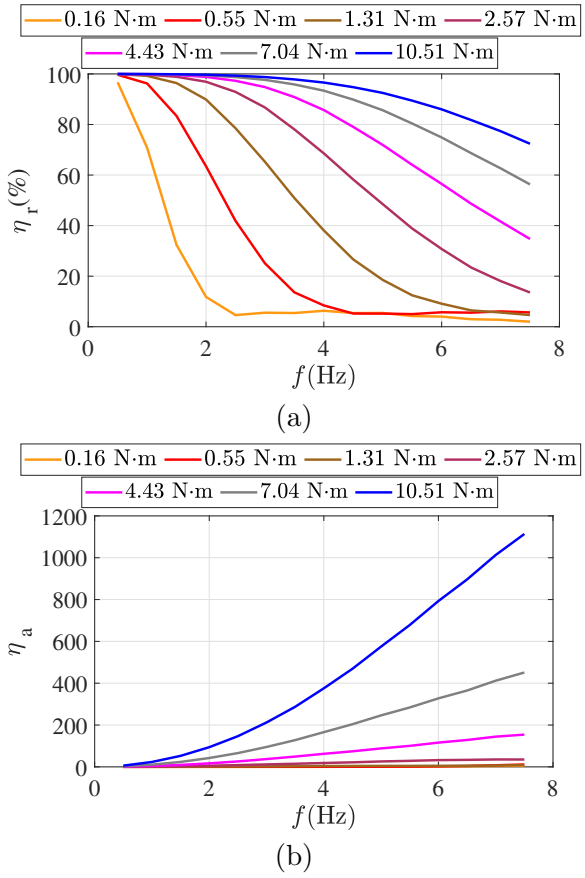


Figure 17. (a) Relative decline ratio and (b) absolute decline value of the variance $\delta^2_{P_m}$ of motor power

Finally, the average power of the motor for different combinations of f and κ_2 is explored, as shown in **Figure 19**. $\bar{P}_m$ increases as f and κ_2 increase, and the maximum $\bar{P}_m$ of 21.53 W is obtained when $f = 7.5$ Hz and $\kappa_2 = 10.51$ N·m. It is obvious that $\bar{P}_m$ will approach the allowable power value of the motor gradually if f and κ_2 increase further, which means that reducing $\delta^2_{P_m}$ and improving the stability of the motor power are essential for protecting the motor from damage.

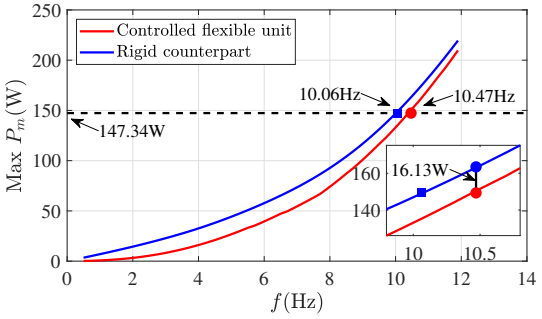


Figure 18. Comparison of the maximum power of the motor between the CFU and rigid counterpart. Here, $\kappa_2 = 10.51$ N·m. The maximum frequencies of the motor for the rigid counterpart and CFU are 10.06 Hz and 10.47 Hz, respectively. Compared with the rigid counterpart, the CFU can lower the maximum motor power by 16.13 W (equivalent to 9.9%).

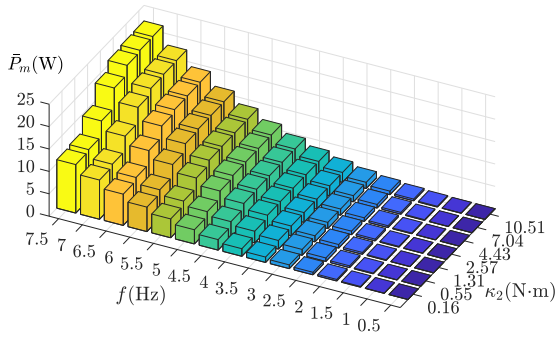


Figure 19. Average motor power $\bar{P}_m$ at different f and κ_2

4.4. Discussion

Based on the above analyses, we can conclude that the CFU's energy storage is incapable of improving the swimming performance of the robotic fish in terms of swimming speed and propulsion efficiency, but is beneficial for improving the stability of the motor power by adjusting the CFU's stiffness reasonably. Moreover, there is an optimal CFU stiffness that can minimize the variance of the motor power for a given frequency and PFU's stiffness, and the optimal CFU stiffness is positively correlated with the peak value of the equivalent joint torque.

In addition, compared with the rigid counterpart, the advantages of the CFU's energy storage can be fully reflected in the improvement of the smoothness of the motor power. On the one hand, it is beneficial to protect the motor from damage and improve the motor's service life. On the other hand, the motor's performance in terms of maximum frequency can be improved effectively. Specifically, in the case of using the same motor, since the rigid counterpart cannot store energy, the peak

power of the motor easily exceeds the allowable value, which limits the maximum average power and frequency. Benefiting from the CFU's energy storage, the motor can achieve higher frequency and average power to improve the swimming performance of the robotic fish without damage by adjusting the CFU's stiffness reasonably.

In addition, regarding the applicability of the optimization model, it mainly includes two aspects. First, the hydrodynamic model of the robotic fish derived in this paper is based on the assumption that the fluid is irrotational and inviscid. Real fluid environments are very complex. Therefore, in the vast majority of hydrodynamic analyses of robotic fish, this widely accepted assumption is adopted. Second, the maximum operating frequency of the dynamic model constructed in this manuscript is 7.5 Hz, which has been validated by experimental data in our previous study.[41]

5. Conclusions and future work

In this paper, we propose a wire-driven elastic robotic fish, whose fishlike tail is based on dual spring steel and includes a CFU and a PFU. As the fishtail swings, the CFU can generate bending deformation under the action of the wire driving and motor, to realize periodic energy storage. We analyzed and verified that the CFU's energy storage and stiffness do not contribute to the swimming performance of the robotic fish, but can affect the smoothness of the motor power. Hence, with the aim of minimizing the variance of the output power of the motor, we optimized the CFU's stiffness by the developed nonlinear optimization model that is based on the Lagrangian dynamics and cantilever beam model. The results show that, compared with the rigid counterpart, the optimized CFU can effectively smooth the motor power, and reduce the peak value as well as the variance of the motor power. Hence, the motor power does not easily exceed the allowable power value , which is beneficial to protect the motor from damage and improve the service life of the motor.

The nonlinear optimization model proposed herein provides a stiffness adjustment strategy for the CFU of robotic fish. The real-time adaptation of the CFU's stiffness based on operating frequency and PFU's stiffness, enabled by variable stiffness technology, is key to maintaining stable motor power output and improving real-world applicability. However, realizing the capability of variable stiffness poses a significant future challenge. Potential solutions, such as shape memory alloys, electrorheological fluids, or antagonistic cables, offer promising avenues for achieving tunable CFU stiffness.

Acknowledgments

None.

Fundings

This work was supported in part by the National Natural Science Foundation of China (Grant No. 62503470), and in part by the Postdoctoral Fellowship Program of China Postdoctoral Science Foundation under Grant Number GZC20251177.

Conflict of interest

The authors declare they have no competing interests.

Author contributions

Conceptualization: Xiaocun Liao, Chao Zhou
Formal analysis: Chao Zhou
Funding acquisition: Xiaocun Liao, Chao Zhou
Investigation: Xiaocun Liao, Zhaoran Yin
Methodology: Xiaocun Liao
Project administration: Chao Zhou
Resources: Xiaocun Liao
Software: Xiaocun Liao, Zhuoliang Zhang
Supervision: Chao Zhou
Validation: Xiaocun Liao
Writing - original draft: Xiaocun Liao
Writing - review & editing: All authors

Availability of data

Not applicable.

AI tools statement

All authors confirm that no AI tools were used in the preparation of this manuscript.

References

1. Chen Y, Ren T, Li Y, *et al.* AI-empowered intelligence in industrial robotics: technologies, challenges, and emerging trends. *Intell Robot.* 2026;6(1):1-18. https://doi.org/10.20517/ir.2026.01

2. Li K, Yang L, Cheng Q, Wang B, Xu L. Magnetic soft robots in biomedicine: From remote actuation to diagnostic-therapeutic integrated systems. *Adv Bionics.* 2026;2(1):14-32. https://doi.org/10.1016/j.abs.2026.01.001

3. Wang J, Wang C, Chen W, Dou Q, Chi W. Embracing the future: the rise of humanoid robots and embodied AI. *Intell Robot.* 2024;4(2):196. https://doi.org/10.20517/ir.2024.12

4. Sun Y, Yan C, Xiang X, Zhou H, Tang D, Zhu Y. Towards end-to-end formation control for robotic fish via deep reinforcement learning with non-expert imitation. *Ocean Eng.* 2023;271:113811. https://doi.org/10.1016/j.oceaneng.2023.113811

5. Dai W, Rai U, Chiun J, Cao Y, Sartoretti G. Heterogeneous multi-robot task allocation and scheduling via reinforcement learning. *IEEE Robot Autom Lett.* 2025;10(3):2654-2661. https://doi.org/10.1109/LRA.2025.3534682

6. He H, Liao R, Li Y. MSAFNet: a novel approach to facial expression recognition in embodied AI systems. *Intell Robot.* 2025;5(2):313-332. https://doi.org/10.20517/ir.2025.16

7. Zheng X, Wang W, Xiong M, Xie G. Online state estimation of a fin-actuated underwater robot using artificial lateral line system. *IEEE Trans Robot.* 2020;36(2):472-487. https://doi.org/10.1109/TRO.2019.2956343

8. Zhang Y, Zhu D, Chen M, Yang SX. Model predictive tracking control based on adaptive sliding mode constraints for unmanned underwater vehicles. *Intell Robot.* 2026;6(1):101-119. https://doi.org/10.20517/ir.2026.06

9. Hua M, Zhou W, Cheng H, Chen Z. Improved DDPG algorithm-based path planning for unmanned surface vehicles. *Intell Robot.* 2024;4(4):363-384. https://doi.org/10.20517/ir.2024.22

10. Scaradozzi D, Palmieri G, Costa D, Pinelli A. BCF swimming locomotion for autonomous underwater robots: A review and a novel solution to improve control and efficiency. *Ocean Eng.* 2017;130:437-453. https://doi.org/10.1016/j.oceaneng.2016.11.055

11. Zhang P, Wu Z, Meng Y, Tan M, Yu J. Nonlinear model predictive position control for a tail-actuated robotic fish. *Nonlinear Dyn.* 2020;101(4):2235-2247. https://doi.org/10.1007/s11071-020-05963-2

12. Omari M, Ghommem M, Romdhane L, Hajj MR. Performance analysis of bio-inspired transformable robotic fish tail. *Ocean Eng.* 2022;244:110406. https://doi.org/10.1016/j.oceaneng.2021.110406

13. Clapham RJ, Hu H. iSplash: Realizing fast carangiform swimming to outperform a real fish. In: *Robot Fish: Bio-inspired Fishlike Underwater Robots*. Springer; 2015:193-218. https://doi.org/10.1007/978-3-662-46870-8_7

14. Liu S, Wang Y, Li Z, Jin M, Ren L, Liu C. A fluid-driven soft robotic fish inspired by fish muscle architecture. *Bioinspir Biomim.* 2022;17(2):026009. https://doi.org/10.1088/1748-3190/ac4afb

15. Aubin CA, Choudhury S, Jerch R, Archer LA, Pikul JH, Shepherd RF. Electrolytic vascular systems for energy-dense robots. *Nature.* 2019;571(7763):51-57. https://doi.org/10.1038/s41586-019-1313-1

16. Marchese AD, Onal CD, Rus D. Autonomous soft robotic fish capable of escape maneuvers using fluidic elastomer actuators. *Soft Robot.* 2014;1(1):75-87. https://doi.org/10.1089/soro.2013.0009

17. Katzschmann RK, DelPreto J, MacCurdy R, Rus D. Exploration of underwater life with an acoustically controlled soft robotic fish. *Sci Robot.* 2018;3(16):eaar3449. https://doi.org/10.1126/scirobotics.aar3449

18. Wang Z, Hang G, Wang Y, Li J, Du W. Embedded SMA wire actuated biomimetic fin: A module for biomimetic underwater propulsion. *Smart Mater Struct.* 2008;17(2):025039. https://doi.org/10.1088/0964-1726/17/2/025039

19. Li L, Guo X, Liu Y, Zhang D, Liao WH. Dynamic modeling of a fish tail actuated by IPMC actuator based on the absolute nodal coordinate formulation. *Smart Mater Struct.* 2022;31(11):115005. https://doi.org/10.1088/1361-665X/ac8c0a

20. Li G, Chen X, Zhou F, *et al.* Self-powered soft robot in the Mariana Trench. *Nature.* 2021;591(7848):66-71. https://doi.org/10.1038/s41586-020-03153-z

21. Ning K, Hartono P, Sawada H. Using inverse learning for controlling bionic robotic fish with SMA actuators. *MRS Adv.* 2022;7(30):649-655. https://doi.org/10.1557/s43580-022-00328-w

22. Chen X, Yu J, Wu Z, Meng Y, Kong S. Toward a maneuverable miniature robotic fish equipped with a novel magnetic actuator system. *IEEE Trans Syst Man Cybern Syst.* 2018;50(7):2327-2337. https://doi.org/10.1109/TSMC.2018.2812903

23. Huang C, Lai Z, Zhang L, Wu X, Xu T. A magnetically controlled soft miniature robotic fish with a flexible skeleton inspired by zebrafish. *Bioinspir Biomim.* 2021;16(6):065004. https://doi.org/10.1088/1748-3190/ac23a9

24. Chen B, Jiang H. Swimming performance of a tensegrity robotic fish. *Soft Robot.* 2019;6(4):520-531. https://doi.org/10.1089/soro.2018.0079

25. Chen B, Jiang H. Body stiffness variation of a tensegrity robotic fish using antagonistic stiffness in a kinematically singular configuration. *IEEE Trans Robot.* 2021;37(5):1712-1727. https://doi.org/10.1109/TRO.2021.3049430

26. Li Z, Zhong Y, Du R. A novel underactuated wire-driven robot fish with vector propulsion. In: *2013 IEEE/RSJ International Conference on Intelligent*

Robots and Systems. 2013:941-946.
https://doi.org/10.1109/IROS.2013.6696463

27. Zhong Y, Li Z, Du R. A novel robot fish with wire-driven active body and compliant tail. *IEEE/ASME Trans Mechatron*. 2017;22(4):1633-1643.
https://doi.org/10.1109/TMECH.2017.2712820

28. Liu J, Zhang C, Liu Z, *et al*. Design and analysis of a novel tendon-driven continuum robotic dolphin. *Bioinspir Biomim*. 2021;16(6):065002.
https://doi.org/10.1088/1748-3190/ac2126

29. Shintake J, Zappetti D, Peter T, Ikemoto Y, Floreano D. Bio-inspired tensegrity fish robot. In: *2020 IEEE International Conference on Robotics and Automation (ICRA)*. 2020:2887-2892.
https://doi.org/10.1109/ICRA40945.2020.9196675

30. Estarki M, Varnousfaderani RH, Ghafarirad H, Zareinejad M. Design and implementation of a soft robotic fish based on carangiform fish swimming. In: *2021 9th RSI International Conference on Robotics and Mechatronics (ICRoM)*. 2021:322-328.
https://doi.org/10.1109/ICRoM54204.2021.9663484

31. Park YJ, Jeong U, Lee J, Kim HY, Cho KJ. The effect of compliant joint and caudal fin in thrust generation for robotic fish. In: *2010 3rd IEEE RAS & EMBS International Conference on Biomedical Robotics and Biomechatronics*. 2010:528-533.
https://doi.org/10.1109/BIOROB.2010.5626007

32. Reddy S, Sen S, Har C. Effect of flexural stiffness distribution of a fin on propulsion performance. *Mech Mach Theory*. 2018;129:218-231.
https://doi.org/10.1016/j.mechmachtheory.2018.07.012

33. Chen D, Wu Z, Meng Y, Tan M, Yu J. Development of a high-speed swimming robot with the capability of fish-like leaping. *IEEE/ASME Trans Mechatron*. 2022;27(5):3579-3589.
https://doi.org/10.1109/TMECH.2021.3136342

34. Behbahani SB, Tan X. Design and modeling of flexible passive rowing joint for robotic fish pectoral fins. *IEEE Trans Robot*. 2016;32(5):1119-1132.
https://doi.org/10.1109/TRO.2016.2593452

35. Li Z, Du R, Zhang Y, Li H. Robot fish with novel wire-driven continuum flapping propulsor. *Appl Mech Mater*. 2013;300:510-514.
https://doi.org/10.4028/www.scientific.net/AMM.300-301.510

36. Lau WP, Zhong Y, Du R, Li Z. Bladderless swaying wire-driven robot shark. In: *2015 IEEE 7th International Conference on Cybernetics and Intelligent Systems (CIS) and IEEE Conference on Robotics, Automation and Mechatronics (RAM)*. 2015:155-160.
https://doi.org/10.1109/ICCIS.2015.7274613

37. Fujiwara S, Yamaguchi S. Development of fishlike robot that imitates carangiform and subcarangiform swimming motions. *J Aero Aqua Bio-mech*. 2017;6(1):1-8.
https://doi.org/10.5226/jabmech.6.1

38. El Daou H, Salumäe T, Toming G, Kruusmaa M. A bio-inspired compliant robotic fish: Design and experiments. In: *2012 IEEE International Conference on Robotics and Automation*. 2012:5340-5345.
https://doi.org/10.1109/ICRA.2012.6225321

39. Valdivia y Alvarado P, Youcef-Toumi K. Design of machines with compliant bodies for biomimetic locomotion in liquid environments. *J Dyn Syst Meas Control*. 2006;128:3-13.
https://doi.org/10.1115/1.2168476

40. Jiang Y, Liu X, Chen H, Gong W, Lu Y, Zhang W. Design and modeling of a biomimetic wire-driven soft robotic fish. In: *2019 Chinese Automation Congress (CAC)*. 2019:1778-1782.
https://doi.org/10.1109/CAC48633.2019.8996663

41. Liao X, Zhou C, Wang J, Tan M. A wire-driven dual elastic fishtail with energy storing and passive flexibility. *IEEE/ASME Trans Mechatron*. 2023;29(3):1914-1925.
https://doi.org/10.1109/TMECH.2023.3318219

Xiaocun Liao *received the B.E. degree in Detection, Guidance, and Control Technology from Central South University (CSU), Changsha, China, in 2019, and the Ph.D. degree in Control Theory and Control Engineering from the Institute of Automation, Chinese Academy of Sciences (IACAS), Beijing, China, in 2024. He is currently an Associate Professor with the Key Laboratory of Cognition and Decision Intelligence for Complex Systems, IACAS. His research interests include robotic design and control, etc.*
https://orcid.org/0000-0002-9455-7015

Chao Zhou *received the B.E. degree in automation from Southeast University, Nanjing, China, in July 2003, and the Ph.D. degree in control theory and control engineering from the Institute of Automation, Chinese Academy of Sciences (IACAS), Beijing, China, in 2008. He is currently a Professor with the State Key Laboratory of Management and Control for Complex Systems, IACAS. His research interests include robot motion control, bioinspired robotic fish, and embedded robot systems.*
https://orcid.org/0000-0003-4461-8075

Junfeng Fan *received the B.S. degree in mechanical engineering and automation from Beijing Institute of*

Technology, Beijing, China, in 2014 and the Ph.D. degree in control theory and control engineering from the Institute of Automation, Chinese Academy of Sciences (IACAS), Beijing, China, in 2019. He is currently an Associate Professor in Control Theory and Control Engineering with the State Key Laboratory of Management and Control for Complex Systems, IACAS, Beijing. His research interests include robot vision and underwater robots.
https://orcid.org/0000-0003-4922-7946

Zhuoliang Zhang *received the B.E. degree in automation from Tongji University, Shanghai, China, in July 2018, and the Ph.D. degree in control theory and control engineering from the Institute of Automation, Chinese Academy of Sciences (IACAS), Beijing, China, in June 2023. He is currently a Post doctoral Fellow with the Laboratory of Cognition and Decision Intelligence for Complex Systems, IACAS. His research interests include measurements, sensor signal processing, and intelligent control.*
https://orcid.org/0000-0002-5991-2392

Zhaoran Yin *received the B.E. degree in automation from the School of Control Science and Engineering, Shandong University, Jinan, China, in 2017, and the M.S. degree in Electrical Engineering from the University of Texas at Dallas, Richardson, TX, USA. He is currently working toward the Ph.D. degree in control theory and control engineering with the Institute of Automation, Chinese Academy of Sciences (IACAS), Beijing, China. His research interests include bioinspired underwater robots and intelligent control systems.*
https://orcid.org/0000-0003-1643-3495

Liangwei Deng *received the B.E. degree in mechanical design, manufacturing, and automation from the University of Electronic Science and Technology of China (UESTC), Chengdu, China, in 2020. He is currently working toward the Ph.D. degree in control theory and control engineering with the Institute of Automation, Chinese Academy of Sciences (IACAS), Beijing, China. His research interests include bioinspired robots.*
https://orcid.org/0000-0002-2416-8815

An International Journal of Optimization and Control: Theories & Applications (https://accscience.com/journal/ijocta)

This work is licensed under a Creative Commons Attribution 4.0 International License. The authors retain ownership of the copyright for their article, but they allow anyone to download, reuse, reprint, modify, distribute, and/or copy articles in IJOCTA, so long as the original authors and source are credited. To see the complete license contents, please visit http://creativecommons.org/licenses/by/4.0/.